Surface and Electronic Structure of Titanium Dioxide Photocatalysts

S. A. Bilmes*,† and P. Mandelbaum

INQUIMAE-Departamento de Química Inorgánica, Analítica y Química-física, Facultad de Ciencias Exactas y Naturales, Universidad de Buenos Aires, Ciudad Universitaria Pab. II, C1428EHA Buenos Aires, Argentina

F. Alvarez*,‡ and N. M. Victoria

Instituto de Física "Gleb Wataghin", Universidade Estadual de Campinas Unicamp, 13083-970 Campinas, São Paulo, Brazil

Received: March 16, 2000; In Final Form: July 21, 2000

TiO_2 films prepared by sol−gel route are active photocatalysts for the oxidation of organics in photoelectrochemical cells. The as-grown films for photocatalysis applications and those exposed to Ar^+ or H_2^++Ar^+ ion bombardment are characterized by different spectroscopic methods, such as X-ray diffraction (XRD), atomic force microscopy (AFM), UV−vis transmittance, photothermal deflection spectroscopy (PDS) and X-ray photoelectron spectroscopy (XPS), as well as by conductance. This material has defects associated with oxygen vacancies produced during the sample preparation which support nondissociative adsorption of O_2 when films are exposed to air. Charge transfer from reduced Ti species to adsorbed dioxygen leads to Ti−O_2^- surface complexes that are partially removed by heating at 200 °C, and fully removed after 30 min ion bombardment. By comparison with the relatively well-understood structural defects of bombarded TiO_2 we arise to a quite complete structural model of the as grown material which corresponds to an amorphous semiconductor possessing relative low disorder and density of states as compared with a pure amorphous material. These TiO_2 films are modeled as low size crystalline domain embedded in an amorphous matrix whose electronic structure exhibit exponential band tails and a narrow band close to the conduction band. The latter is fully or partially occupied depending on the presence of adsorbed electron scavengers such as dioxygen.

Introduction

The need of new and effective methods for cleaning polluted air or water has prompted considerable efforts in the research for complete mineralization of a wide range of dissolved or dispersed organic compounds. Since the pioneering work of Carey et al.,[1] heterogeneous photocatalysis has been proven for decomposition of many organic compounds, conversion of inorganic anions, and metal removal by photochemical reduction.[2−5] Several commercial devices have been developed for decontamination of air,[6] but the low quantum yield of most photocatalytic oxidation reactions in aqueous systems translates into comparatively high power costs. The efficiency of the overall process decreases as the catalyst is immobilized,[7] and it is not clear whether the interfacial structure or mass-transfer limitations can account for these differences. However, the fact that the photodegradation rate can be improved with TiO_2 films under bias in a photoelectrochemical cell[8−11] provides evidence that interfacial charge-transfer processes play an important role. Thus, one fundamental question that is still open[12] concerns to the structure of the TiO_2 film/electrolyte interface which in turn, is determined by the electrolyte composition, and the semiconductor surface composition and electronic structure.

The interest of TiO_2 films exceeds photocatalytic applications and they are widely used as optical coatings and sensors.[13−15] Their synthesis by sol−gel route has been proved to be effective for producing photocatalysts operating under bias,[10,11] for use in solar cells,[16,17] self-cleaning windows,[18] and electrochromic devices.[19] The TiO_2 surface is covered by adsorbates, mainly dioxygen and water from the surrounding environment, which play an important role in interfacial charge transfer: water adsorbs dissociatively giving rise to efficient hole traps, such as surface −OH, and dioxygen is an efficient electron scavenger in nonaqueous media.[14,20−25] From the structural point of view, these materials are usually nanocrystalline structured in a network of mesoscopic oxide particles,[26−29] implying their electronic structure description need to include localized states from defects and grain boundaries, as well as band tails in the gap.

The ideal TiO_2 (110) surface contains 5-fold Ti^{4+} coordinated to O^{2-}, but even at room temperature a *real* surface has a non negligible density of oxygen vacancies which give rise to localized defects of Ti^{2+} and Ti^{3+}.[20,30,31] The presence of reduced Ti species on the surface and underneath plays an important role in adsorption.[20] In particular, for the adsorption of dioxygen it has been demonstrated that both molecular and dissociative channels occur at defects with charge transfer from reduced Ti.[20,25,32−35] On the other hand, little is known about the structure of TiO_2 films and their interfaces in air or in aqueous electrolytes;[12,37,38] it is expected that crystallinity, density of defects, and electronic structure depend on the interaction with the substrate, synthesis pathway, and thermal treatment variables. Then, to develop an efficient photocatalysts for air or water

* Corresponding authors.
† E-mail: sarabil@q3.fcen.uba.ar.
‡ E-mail: alvarez@ifi.unicamp.br.

10.1021/jp0010132 CCC: $19.00 © 2000 American Chemical Society
Published on Web 10/03/2000

detoxification it is mandatory an exhaustive structural characterization of the TiO_2 film forming the semiconductor/electrolyte interface.

In this work we present a comprehensive study containing results on the surface structure, chemical composition, optical absorption and electric transport for TiO_2 films prepared by sol−gel route that are active photocatalysts for the oxidation of organics in photoelectrochemical cells.[11,39] The as-grown films for photocatalysis applications are characterized by different spectroscopies methods, such as X-ray diffraction (XRD), atomic force microscopy (AFM), UV−vis transmittance, photothermal deflection spectroscopy (PDS), and X-ray photoelectron spectroscopy (XPS). The conductance of the samples was also measured. These results are compared with those obtained for the same films exposed to Ar^+ or H_2^++Ar^+ ion bombardment. Moreover, by a comparison with the relatively well understood structural defects of bombarded TiO_2 we arise to a quite complete structural model of the as-grown material.[33,40−42]

Materials and Methods

Synthesis of Films. Titanium dioxide films were prepared by the sol−gel route. Sols prepared by hydrolysis of Ti(IV) butoxide at pH < 1 were dialyzed against water up to pH 3.4. The resulting gel was spin coated either onto quartz or onto conducting indium−tin oxide (ITO) glass and heated at 90 °C for 5 min. This procedure was repeated six times; after the sixth deposit, the assembly was sintered 6 h at 400 °C in air. The thickness of each layer was 50 nm, as determined by AFM images of the partially covered substrate in which a defined step was formed by removing a strip of Scotch tape previously adhered. The average thickness of the films was (300 ± 50) nm as determined by profilometry and by atomic force microscopy (AFM).

Experimental Methods. X-ray diffractograms were obtained with a Siemens D5000 operating with Cu Kα radiation source filtered with a graphite monochromator (λ = 1.5406 Å). The incidence angle was 3°, and both emission and detection slits were 1 mm. The length of the crystalline domain was calculated by Scherrer equation[43] with an instrumental factor of 0.03°.

AFM images were obtained with a PSI Autoprobe CP with a 5 μm Si contact ultralever scanner. All scans were run in contact regime at 10 pN and 2 Hz. The RMS roughness of the surface was calculated as a standard deviation on the *z*-scale with the PSI program.

All the X-ray photoemission spectra were taken at room temperature with a Vacuum Generator (VG) CLAMP 3 (0.3 eV resolution) operating in the constant-analyzer-energy mode in a UHV chamber (<10^{-9} mb) using the Al Kα line (VG XR3 X-ray source, $h\nu$ = 1486.6, width 0.85 eV). The mirror analyzer pass energy was 10 eV. The binding energies were calibrated with reference to sputtered cleaned Ag standard. To confirm that prolonged evacuation does not modify the surface chemical composition, several test spectra were taken over 14 h. The XPS chamber is attached in-line with that for ion treatment in such a way of allowing in situ bombardment experiments. The bombardment experiments were performed by using a Kaufman cell feeding with Ar or a H_2 + Ar mixture with energies 100 eV and a current density of 10 mA.cm^{-2}. More experimental details of the treatment chamber are published elsewhere.[44]

UV−vis transmittance spectra of films deposited onto quartz were taken with a single beam spectrophotometer (Perkin-Elmer λ9). High sensitive spectra in the 310−850 nm range were taken in a standard photothermal deflection spectroscopy (PDS) system. In PDS experiments, the sample was irradiated with chopped monochromatic light from a 1000 W Xe lamp. CCl_4 was employed as deflecting medium, and the in phase deflection of the He−Ne laser was detected with a photodiode.[45] The complete spectra in the 310−850 nm range were obtained by matching the PDS and transmittance spectra in the 3.5−3.7 eV region. Since the PDS is an optical absorption relative measurement, scaling the PDS with the visible spectra is a standard procedure.[46]

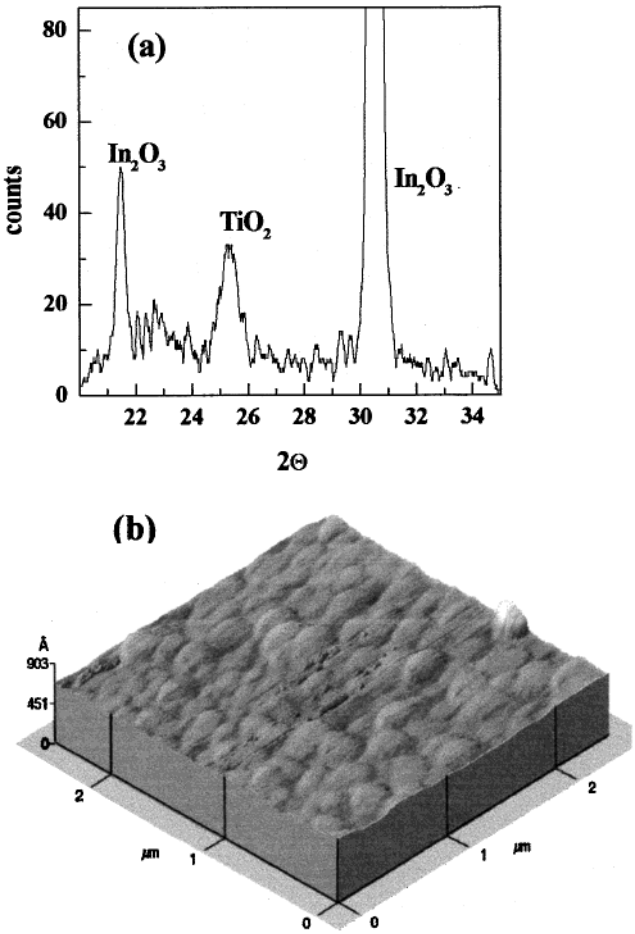

Figure 1. (a) DRX spectrum of TiO_2 films 300 nm thick deposited onto ITO. (b) AFM image for the same film.

Conductance measurements of films deposited onto quartz were performed with 1 mm gap and 10 mm wide coplanar evaporated Al contacts. The conductivity was calculated assuming uniform slab of material between the two aluminum strip contacts.

Results

TiO_2 Films as-Grown for Photocatalysis. Figure 1.a shows the X-ray difractogram of TiO_2 film deposited onto ITO substrate. The broad peak at 2θ = 25.3 is assigned to anatase structure, and those at 21.5 and 30.5 to the indium oxide from present in the substrate. The size of crystalline domains is (10 ± 2) nm, as determined from the half width anatase peak by Scherrer equation. AFM images (Figure 1b) show a surface structure composed by grains with (300 ± 50) nm average size, twice the average grain size of the ITO substrate. AFM images recorded after deposition of each layer show that roughness decreases from that of ITO on increasing fim thickness. Parameters from AFM for the naked substrate, one-layer and six-layer deposit is shown in Table 1.

TABLE 1: Parameters from AFM Image Analysis for TiO_2 Films Grown for Photocatalysis

	rms roughness (Å)	real area/ geometric area	grain size(nm)
I TO substrate	50 ± 10	1.2 ± 0.1	150 ± 30
one-layer TiO_2	40 ± 10	1.1 ± 0.1	200 ± 30
six-layer TiO_2	20 ± 5	1.02 ± 0.02	300 ± 50

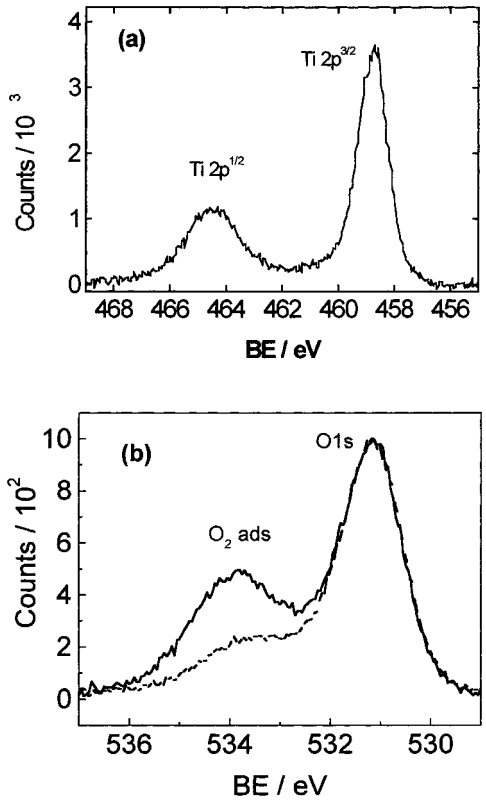

Figure 2. XPS spectrum of TiO_2 films grown for photocatalysis in the Ti 2p (a) and O 1s (b) binding energy (BE) regions. Dashed line in (b) is the spectrum recorded after 30 min at 200 °C.

Figure 2 shows characteristic XPS spectra for a photocatalytic TiO_2 film in the Ti2p (Figure 2a) and O 1s (Figure 2b) electron binding energy regions. Peaks at 458.7 and 464.5 eV correspond to $2p^{3/2}$ and $2p^{1/2}$ core-levels of Ti(IV) bound to oxygen, respectively.[34,41,47] Both peaks are symmetric, and FWHM of $Ti2p^{3/2}$ is 1.25 eV, as in data reported either for "defect-free"-TiO_2 (110) or for TiO_2 films prepared by sol−gel.[34,48] In the O 1s binding energy region, the peak at 530.9 eV corresponds to O 1s core-level of oxygen atoms bound to Ti(IV),[34,48] whereas that at 533.7 eV can be tentatively assigned to adsorbed dioxygen. The latter can be partially removed by heating at 200 °C (dashed line in Figure 2.b), procedure that has no influence on the height, width and location of other XPS peaks. The O/Ti ratio calculated by integration of O 1s (530.9 eV) and Ti2p bands, taking into account the sensitivity factor of each element is 1.9.[49] It should be noted that no carbon from atmospheric or other organic contamination was detected after introducing the samples in the UHV chamber for XPS analysis and reaching the working vacuum ($<1 \times 10^{-9}$ mb), and no signals from In or Sn were measured ruling out the possibility of pinholes.

The UV−vis spectrum of TiO_2 films deposited on quartz obtained by matching the PDS and transmittance spectra in the 3.5−3.7 eV region is shown in Figure 3 (square). In a semiconductor containing gap-states, the absorption spectrum has three well-defined regions referred to the energy gap, E_g:[50] (a) $E > E_g$, corresponding to deep transitions between valence and conduction bands states; (b) an intermediate, and in some cases, near exponential region at $E \approx E_g$, with absorption due to the convolution of optical transitions from valence band states to localized conduction band-tail states (or from localized valence band-tail states to conduction band states); and (c) $E < E_g$ due to transitions from valence band states to localized mid-gap states (or from localized mid-gap states to conduction band states).

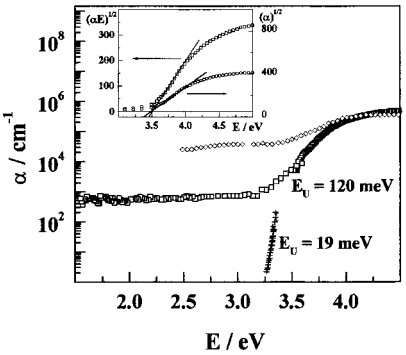

Figure 3. UV−vis spectrum of TiO_2 films grown for (□) photocatalysis. Inset: plots for (left) indirect and (right) Tauc functions. For the sake of comparison, spectra for a rutile crystal at (+) 10 K[53] and for an amorphous (◇) TiO_2 film[54] are also plotted.

The elucidation of what type of mechanism is governing the different parts of the absorption spectrum in TiO_2 (Figure 3, square symbols) is not an easy task. The existence of mid-gap states and a fairly well defined exponential tail strongly suggests characteristics commonly found in amorphous semiconductors.[50] As it is well-known, region (a) of the absorption spectra determine the semiconductor optical gap. In the attempt to identify the most probable type of optical transitions we have plotted $\alpha^{1/2}$ vs $h\nu$ and $(\alpha h\nu)^{1/2}$ vs $h\nu$. These plots are adequate to describe the spectra of crystalline[51] and amorphous[52] materials, respectively. The two procedures lead to the similar gap energy value ($E_g = 3.5$ eV, inset Figure 3) close to that reported for amorphous $TiO_{1.92}$ films.[54] However, the curve representing indirect transitions expand for a shorter range of values suggesting that this mechanism is less probable to represent the actual transitions. Assuming that the intermediate region ($3.2 < E < 3.7$ eV) corresponds to region (b) discussed above, the associated slope of the absorption curve defines the Urbach energy, $E_U = [\mathrm{d} \ln \alpha/\mathrm{d}(h\nu)]^{-1} = 120$ meV.[50] This parameter is generally accepted as a measure of the material disorder. For the sake of comparison, Figure 3 includes data for a rutile crystal at 10 K reported by Tang,[53] and for an amorphous TiO_2 film grown by reactive sputtering.[54] It is interesting to note that TiO_2 films active in photocatalysis are mid way between these two limits; the Urbach energy is approximately six-fold larger than that of the crystal, and the absorption values of the amorphous film in the subgap region is roughly 2 orders of magnitude larger.

Room-temperature conductivity of TiO_2 films as grown for photo- and photoelectrocatalysis is relatively low in air, $\sigma = 10^{-8}\ \Omega^{-1}\mathrm{cm}^{-1}$. This value is similar to those found for amorphous films prepared by sol−gel,[26,48] and approximately 3 orders of magnitude lower than those of crystalline films.[55] Figure 4 shows log σ vs $1/T$ plots measured in the 298K − 410 K temperature range in air (circles) and at 10^{-3} Torr (squares). Heating in air up to 410 K does not improve conductivity, but it increases after the chamber evacuation to 10^{-3} Torr. Conductance becomes thermally activated at the lower pressure (Figure 4, branch I), and heating 40 min at 410 K at 10^{-3} Torr raises the conductivity up to 3 orders of magnitude. Cooling

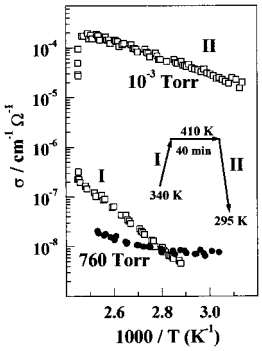

Figure 4. Conductivity change with temperature for as grown TiO_2 films in (●) air and at (□) 10^{-3} Torr. Branches labeled I and II in the plot at 10^{-3} Torr correspond to the temperature program inset in the figure.

down the sample up to 295 K reduces the conductivity in an activated fashion from 2×10^{-4} to 2×10^{-5} cm Ω^{-1} (Figure 4, branch II). The abrupt increase in conductivity upon heating at 10^{-3} Torr is reversed in few seconds (below our measuring time window) by further exposure to air.

Ion Bombarded TiO_2 Films. Low energy ion bombardments of TiO_2 are widely used for producing compositional changes by preferential sputtering of oxygen, inducing damage, disorder, and reducing species.[33,40−42] TiO_2 films as grown for photoelectrocatalysis also exhibit drastic changes upon Ar^+ or $Ar^+-H_2^+$ ion bombardment. The effect of bombardment on the X-ray photoelectron spectra is the broadening of the bands corresponding to Ti 2p core levels (Figure 5a) and to a lower extent that corresponding to O 1s electrons (Figure 5b). The broadening of Ti 2p peaks is also found in ion bombarded crystalline TiO_2 (110), and has been attributed to the formation of Ti species with higher density of negative charge, i.e., Ti^{3+} and Ti^{2+}.[34,56] The energy of the O 1s core-level of oxygen atoms bound to Ti remain at the same energy as the sample is bombarded. On the other hand, the peak assigned to adsorbed O_2 diminishes and shifts to higher energies on ion bombardment (Figure 5b).

The fraction of each Ti species X_{Ti} was determined from the ratio of areas obtained by a deconvolution of their contribution to the overall spectra (Figure 5a, inset). This procedure was done assuming that all bands are Gaussian, have the same fwhm, and that the area under the peak assigned to $2p^{3/2}$ (458.7 eV) core level is twice that of corresponding to $2p^{1/2}$ (464.5 eV).[47] The location found for Ti^{2+} ($2p^{3/2}$, 460.8 eV; $2p^{1/2}$, 455.4 eV) and Ti^{3+} ($2p^{3/2}$, 462.4 eV; $2p^{1/2}$, 457.4 eV) core levels is coincident with that found for other reduced TiO_2 materials.[34,41,47] The evolution of X_{Ti} upon ion bombardment exposure is shown in Figure 6.a. After 3 min ion bombardment the composition of the (reduced) surface saturates to 40% Ti^{4+} and 60% reduced Ti (Ti^{3+} and Ti^{2+}). The spectral deconvolution in the O 1s binding energy region was done relaxing the condition of equal FWHM Gaussians (Figure 5b, inset). In this process was not possible to distinguish between oxygen bound to Ti^{3+} or Ti^{2+}, and the peak located at 531.5 eV corresponds to oxygen bound to both reduced Ti species. The fraction of oxygen atoms bound to different Ti species X_O follows the same trend found for Ti species (Figure 6.b), whereas adsorbed dioxygen is completely removed after 30 min of ion bombardment. It is worth to remark that the same results are obtained with different bombardment ion mixtures (Ar^+ or $Ar^+ + H_2^+$), confirming that the main effect of ion bombardment is preferential oxygen sputtering by Ar^+.

The increasing density of defects and disorder upon ion bombardment was probed by the evolution of absorption spectrum. It was found that the film thickness decreases linearly with the time of exposure to the ion beam (ca. 15% for 30 min) and consequently the absorption intensity does decrease. Therefore, to compare the spectra of samples with different thickness, the curves are scaled in the region of highest absorption values ($E > 3.75$ eV). The excellent spectra coincidence in this energy region stems from the fact that ion bombardment does not affect the contribution from band-to-band transitions (Figure 7a). Spectral shape and intensity is independent of the ion beam composition for the same exposure time, in agreement with XPS results. For any beam exposure time E_g has the same value found for the as grown material, indicating that ion bombardment does not produce degeneracy (Burstein effect).

Even thought the Urbach energy cannot be accurately calculated due to the narrow range of linearity for ion bombarded films, it increases upon exposure to ions. This behavior confirms the increasing structural disorder indicated by the broadening of XPS spectra. On the other hand, the relative increasing defect density (N_D) induced by ion bombardment can be estimated by integration of the subband absorption part of the spectra (1.5 eV $< E <$ 3.5 eV). We note, however, that a considerable amount of band-tail states contribute to the subgap absorption curve and must be properly subtracted.[45,57−59] By following the standard procedures applied in amorphous semiconductors, one can write:

$$N_D = B_{1.5\mathrm{eV}} \int^{3.2\mathrm{eV}} \alpha_e \, dE \qquad (1)$$

where B is a parameter related to the oscillator strength of the optical transition and $\alpha_{ex}(E)$ is the absorption coefficient related to transitions to or from defect states with energy in the forbbiden gap. Then

$$\alpha_{ex}(E) = \alpha(E) - \alpha(3.2\ \mathrm{eV}) \exp(h\nu/E_u) \qquad (2)$$

The integration shows that the defect density increases first by a factor ∼4 after 3 min of ion bombardment, remaining practically constant for longer exposures (Figure 7b). Unfortunately, to obtain absolute N_D values this empirical method requires the knowledge of the parameter B. This coefficient must be independently determined by other techniques, such as electron-spin resonance (ESR) in hydrogenated amorphous silicon.[45] In this study because of the lack of knowledge of B values for TiO_2 absolute measure of the film density of states cannot be obtained, and a relative comparison is only possible.

Figure 8 shows the $\sigma - 1/T$ logaritmic plots for the as grown film for photoelectrocatalysis, for different bombardment times. The conductivity in air appreciably increases upon bombardment; independently of ion beam composition, a saturation value is achieved after ∼3 min (inset in Figure 8). Although the absolute conductivity increases, its temperature dependence does not change appreciably, suggesting that the transport mechanism is the same. It is worth noting that bombarded material is unstable and shows an important conductivity hysteresis that was not observed for the as grown material. This unstability accounts for maxima and positive slopes in the curves depicted in Figure 8.

Discussion

Results presented in previous section allow the description of morphology and electronic properties of TiO_2 films, its chemical composition, and its interface in air or under vacuum.

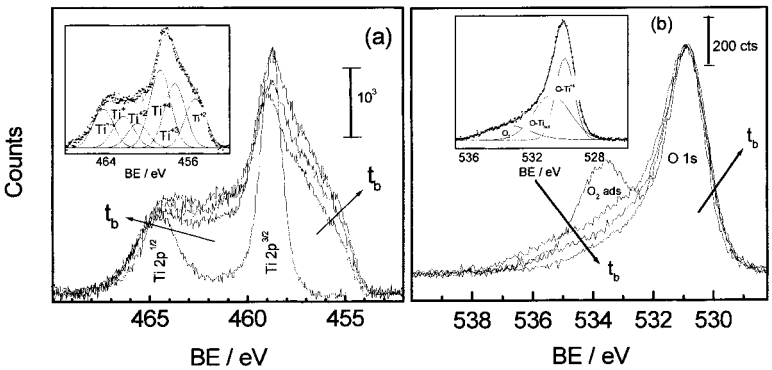

Figure 5. XPS spectra recorded after $t_b = 3$, 15, and 30 min $Ar^+-H_2^+$ beam exposure in the (a) Ti 2p and (b) O 1s binding energy (BE) regions. Arrows indicate the evolution as the bombardment time t_b increases. Spectral deconvolution inset in each figure. Numbers in the spectral deconvolution of Ti 2p express the oxidation number of Ti.

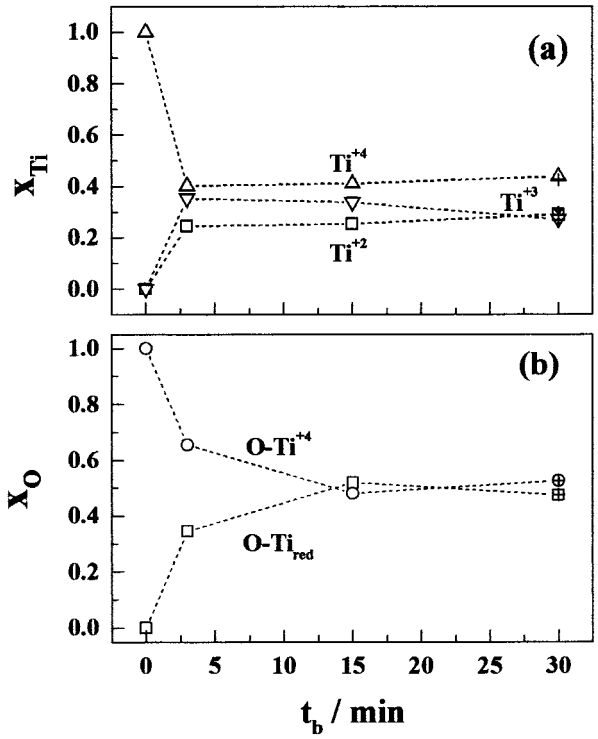

Figure 6. Dependence of surface composition (expresed as atomic fraction, x_i) on bombardment time. (a) Ti species, (b) O species.

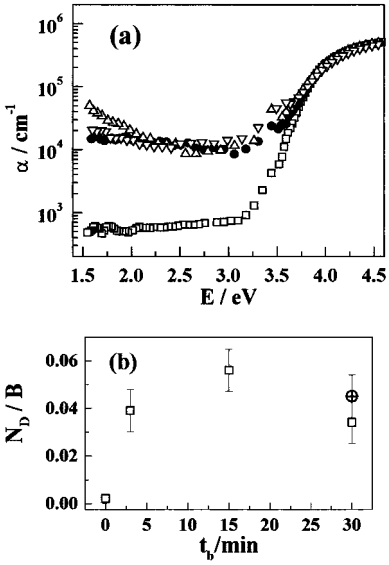

Figure 7. (a) UV-vis spectra recorded after $Ar^+-H_2^+$ beam exposure for (●) 3 min; (▽) 15 min and (△) 30 min. (□) Spectrum recorded before exposure to ion beam. (b) Dependence of defect density (scaled to the parameter *B*, see text) with (□) $Ar^+-H_2^+$ bombardment time t_b. (⊕) Value obtained from experiments with Ar^+ beam.

Crystallinity and Morphology. Films as grown for photoelectrocatalysis are composed by anatase nanocrystals embedded in an amorphous matrix, as concluded from XRD and AFM results shown in Figure 1. This picture is related with the structure of the precursor gel which is composed by a macromolecular network resulting from polymerization of Ti-alkoxide following hydrolysis and condensation reactions[60−63] with crystalline nanoparticles formed in the first steps of hydrolysis and amorphous titania formed by random cross-linking of highly hidroxylated particles and titania oligomers. The final structure of the precursor gel results from the competition between polymerization and particle growth and has large cavities filled with water whose size depends on temperature.[64] Thermal treatment at 90 °C between successive deposits lead to the formation of a more rigid network that can be thought as a "sponge" with cavities bigger than 500−600 Å^3, even water inside the cavities is partially expelled as the cross-linking proceed.[64] The final thermal treatment of the material (electrode) at 450 °C increases water expulsion from cavities and promotes a higher degree of cross-linking, above the percolation threshold, with the resulting assembly fully connected. This temperature is certainly below that corresponding to the amorphous-anatase transition, which lies between 450 and 700 °C,[28,66] and the solid has an important degree of disorder (amorphicity). Within this framework, it can be concluded that grains in AFM images are formed by an amorphous solid which contains small crystallites dispersed in this amorphous matrix. The low crystallinity is further reflected in the penetration (width) of band tails in the gap given by the value of the Urbach energy obtained from Figure 3, which is six times that calculated for anatase single crystals. Although one should expect the presence of pores in the material that would result from the loss of water inside the cavities, none of the techniques employed in this work allow their direct detection.

Chemical Composition. From XPS results for the as grown material (Figure 2) the film surface is composed by Ti^{4+} coordinated to O^{2-} in a 1.9 O:Ti ratio. When considering in the calculation the contribution from the peak at 533.7 eV (Figure 2b) this ratio rises up to 4.5, a value higher than that of a stoichiometric TiO_2 and can be attributed to a surface excess of oxygen. On defective TiO_2 (110) it is generally believed that molecular oxygen is adsorbed as a negative ion.[32,33] Proposed species include superoxide ion O_2^-, peroxide ion O_2^{2-}, and O^-.[20,34] Superoxide and peroxide ions have been detected in photochemical studies involving oxygen and TiO_2 powder in

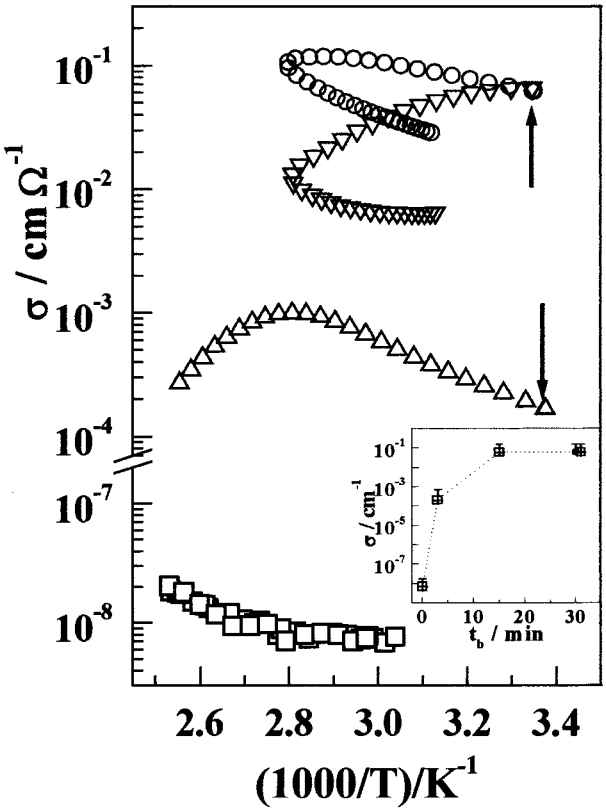

Figure 8. Conductivity dependence on temperature in air for as (□) grown TiO_2 film and for the same film exposed to (△) 3 min, (▽) 15 min, and (○) 30 min $Ar^+-H_2^+$ beam. In all cases runs start at the lowest temperature, as indicated by arrows. Inset: dependence of conductivity at 295 K with (×) $Ar^+-H_2^+$ beam bombardment time. (●) Value obtained from experiments with Ar^+ beam.

air or in an aqueous suspension of the oxide,[2] and the presence of O_2^- species for adsorbed dioxygen on several n-semiconductor oxides has been confirmed byESR.[66,67] Surface O_2^- has similar unpaired electron spin density in both oxygen atoms giving an electron density uniformly distributed over the entire molecular ion. Then, the electron density on each oxygen atom in $Ti-O_2^-$ must be lower than that of those coordinated to two Ti neighbors giving a higher binding energy for the O 1s electron core level, as found.

In a recent paper, Henderson et al.[33] identify O_2^- species adsorbed on Ti(110) at 120 K, desorbing at 410 K with a characteristic stretching frequency and electronic transitions consistent with those of inorganic $Ti-O_2^-$ complexes. In this case, the formation of surface superoxide is associated with the presence of oxygen vacancy sites with enough electron density for transferring the necessary charge to form $Ti-O_2^-$ bonds. Despite the differences between both TiO_2 systems, films grown by sol−gel in air contain O_2 either occluded or adsorbed, then on this defective material there is a considerable density of surface $Ti-O_2^-$ complexes that allow their detection by XPS. Oxygen binding should be stronger than that for O_2 adsorbed onto a clean oriented surface; in agreement, O_2^- is released slowly even at higher temperatures (Figure 5 b). From the area of XPS peaks and taking into account the O_2^- contribution, the O/Ti ratio is 4.5. This value is higher than that expected for the fully covered surface containing each Ti atom bonded to one O_2^-. Although it was suggested that each surface oxygen vacancy site is responsible for binding up to three O_2 molecules,[33] this value may also be assigned to the presence of pores in the material. However, it is not possible to draw a definite conclusion on the presence of pores with diameter enough to support the inclusion of molecular oxygen in the bulk material from XPS experiments sensing 3 nm from the surface.

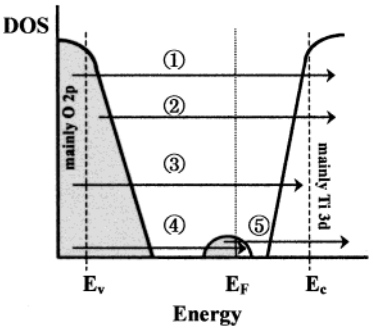

Figure 9. Schematized density of states for TiO_2 films in air and optical transitions described in the text. Dashed lines indicate band tails for a crystal.

O_2^- modifies the density of reduced Ti species and strongly influences charge transport through the film. O_2^- is an efficient electron scavenger,[25] and its presence prevents the detection by XPS of reduced Ti species in the surface layer analyzed. Moreover, even the O(1s)/Ti(2p) ratio of 1.9 indicates the presence of oxygen vacancies, reduced Ti species are found in XPS experiments only after exposure to ion beams that increase the density of defects and structural disorder (Figure 5). Ion bombardment of films used in photoelectrocatalysis removes O_2^-, and the preferential sputtering of O atoms gives rise to oxygen vacancies and to more abundant reduced Ti species, as shown in Figures 5 and 6. On the other hand, partial removal of O_2^- by heating at 200 °C does not increase noticeably the amount of reduced Ti species at the surface, that remain below the detection limit. The fact that XPS results for ion bombarded films and TiO_2 single crystals are coincident reflects the lack of sensitivity of this technique to the long-range environment for each atom.

Electronic Structure. The noncrystallinity of the material employed for photoelectrocatalysis implies that electron distribution exceeds the simplest semiconductor picture of conduction and valence bands separated by an energy gap. The experimental evidences demonstrate the existence of localized states, bands of defects and band-tails penetrating into the forbidden gap, that give rise to the optical transitions schematized in Figure 9. Transition (1) produces optical absorption in region (a) above 3.75 eV; from a chemical point of view this is a O2p → Ti3d charge-transfer transition. Absorption between 3.25 and 3.7 eV (region (b)) is assigned to transitions 2 and 3, i.e., between band tails. Exponential or parabolic band tails are typical of amorphous solids, and the degree of amorphicity can be parametrized by the value of Urbach energy E_U. These band tails result from the distortion of octhaedral units that weakens Ti−O bonds reducing the splitting between bonding and nonbonding levels which give rise to a distribution of states near the band edges. The increase of disorder induced by ion bombardment, among other effects, increases the number of distorted cells, spreading band tails more deeply into the gap and increasing E_U. Although E_U could not be calculated with accuracy for ion bombarded films in Figure 7 its value is close to that for amorphous TiO_{2-x} films produced by reactive sputtering[54] shown in Figure 3.

Another consequence of intrinsic disorder in TiO_2 is the presence of oxygen vacancies and dangling bonds (generalized as defects) that reduce the cation charge and coordination number leading to localized states in the gap. Depending on their density and energy distribution, these states can merge into a midgap band, and allow low energy excitation pathways, as indicated by transitions 4 and 5 in Figure 9. Although localized

states also arise from grain boundaries, their density ratio should be in the order of the crystallite/grain volume ratio (see Figure 1). Absorption below 3.2 eV increases with ion bombardment exposure (Figure 7), following the same trend as the density of reduced Ti species (Figure 5); thus, these bands can be assigned to transitions between occupied and unoccupied Ti 3d orbital (d−d transitions). Occupied Ti3d orbital are Ti^{3+} species associated with adjacent oxygen vacancies V_O, leading to a $2Ti^{3+}-V_O$ complex with poorly screened electrons. Electronic transitions involving these defects on ion bombarded $TiO_2(110)$ surfaces lead to a broad feature in electron energy loss spectra over a range between 0.5 and 2.5 eV,[20,34] in agreement with the absorbance measured in PDS experiments in the subgap region.

In the as grown material Ti^{3+} species are detected by PDS, but not by XPS. The higher penetration depth of visible light makes PDS less sensitive to the removal of surface Ti^{3+} by association with O_2 that leads to $Ti^{4+}-O_2^-$ surface complex.

Electrical Properties. Electron transport in either TiO_2 films active in photocatalysis or modified by ion bombardment can be analyzed on the basis of the electronic structure sketched in Figure 9. The material is a nonstoichiometric n-type semiconductor (TiO_{2-x}), and its conductance depends on the density of donor Ti^{3+} states located close to the conduction band, i.e., ionizable impurities. Assuming full donors ionization, the density of carriers at the conduction band is given by the bulk and/or surface oxygen vacancies. The low slope of $\log(\sigma)$ vs $1/T$ plots is typical of amorphous materials. It markedly differs from the slope observed in polycrystalline, microcrystalline and nanocrystalline TiO_2 films where transport is mainly controlled by the height of intergrain barriers.[55,68] The conductivity dependence on temperature does not change significantly by ion bombardment (Figure 8). This result suggests that bombardment does not alter the transport mechanism by hopping between localized states. Therefore, it is important to elucidate if the observed conductivity changes upon heating or ion bombardment of the as grown TiO_2 film are due to bulk and/or surfaces effects. The penetration depth in our experimental conditions is beyond 200 Å;[69] it can be thought therefore that the oxygen vacancies shown by XPS in Figure 5 (an essentially surface technique) are true bulk features. However, from PDS of ion bombarded films (Figure 7) the increase of defect density is derived to be only about 2 orders of magnitude. To explain the increase in conductivity of over 5 orders of magnitude, it is necessary to consider the conductivity changes due to the depletion region formed beneath the surface by electron scavenging.[25] As discussed above, adsorbed dioxygen is fully removed after 30 min ion bombardment, and half of the initial O_2^- present on the as grown material is removed by heating the sample at 200 °C in a vacuum (Figure 2b). Removing O_2^- under these conditions increases the conductivity by 3 orders of magnitude, as shown in Figure 4. Therefore, one can conclude that for TiO_2 films active in photocatalysis the conductivity is mainly controlled by the space charge layer formed by chemisorption of dioxygen.

As shown in Figure 7b, the density of defects increases first and remains essentially constant after few minutes of ion bombardment. The correlation between density of states and conductivity confirms that an occupied Ti3d narrow band of states is located below the bottom of the conduction band, whose density increases on removing lattice O atoms. Indeed, this is similar to the "tailing" effect found in heavily doped crystalline semiconductors.[51] Therefore, the increasing conductivity on ion doses is associated with two effects: (i) the increasing density of states near to the bottom of the conduction band, and (ii) the increasing population of this band at the surface by O_2 desorption.

Conclusions

The behavior of TiO_2 films prepared by sol−gel is similar to an amorphous semiconductor with low disorder and density of states as compared with a pure amorphous material. The electronic structure, schematized in Figure 9, differs from that of crystalline TiO_2 by the exponential band tails and the existence of a narrow band close to the conduction band. The latter is fully or partially occupied depending on the presence of adsorbed electron scavengers such as dioxygen. The main effect of bombardment is to increase the penetration of band tails into the gap (increase of distorted cells) and the number of states in the narrow band (increase of defects).

Surface oxygen vacancies support non dissociate oxygen adsorption that remove the excess of electrons associated with the vacancies leading to a poorly conducting material. This makes this material as very suitable for air photocatalysis in which the hole transfer to any organic molecule must be accompanied by electron transfer to an appropriate acceptor. However, one expects that in aqueous environment water adsorption removes surface dioxygen, and in consequence efficient photocatalysis for water remediation needs the presence of other electron acceptors or its drift from the surface by an external electric field. The question of the role of gap states and defect band in the efficiency of photocatalysis under bias remains open.

Acknowledgment. Work supported by Grants UBACyT TX-02, CONICET-PIP- 387, and ANPCyT PICT 3844. Exchange between University of Campinas, SP, Brazil, and University of Buenos Aires was partially founded by the network CYTED VIIIG. FAPESP and CNPq supported part of the work in Campinas. The authors thank Marcelo Otero for AFM measurements, Galo Soler Illia and Matías Jobbaggy for XRD measurements, and P. Hammer for assistance with the IBAD deposition system, and Miguel A. Blesa for critical reading of the manuscript.

References and Notes

(1) Carey, J. H.; Lawrence, J.; Tosine, H. M. *Bull. Environ. Contam. Toxicol.* **1976**, *16*, 697.

(2) Serpone, N.; Pellizzetti, E. Eds. *Photocatalysis Fundametals and Applications*; Wiley Interscience: New York, 1989.

(3) Legrini, O.; Braun, A. M.; Oliveros, E. *Chem. Rev.* **1993**, *93*, 671.

(4) Bahnemann, D.; Cunningham, J.; Fox, M. A.; Pelizzetti, E.; Pichat, P.; Serpone, N. *In Aquatic and Surface Photochemistry*; Helz, G., Zepp, R., Crosby, D., Eds.; CRC Press: Boca Raton, 1994.

(5) Hoffmann, M. R.; Martin, S. T.; Choi, W.; Bahnemann, D. W. *Chem. Rev.* **1995**, *95*, 69.

(6) Heller, A. *Acc. Chem. Res.* **1995**, *28*, 503.

(7) Pozzo, R. L.; Baltanás M. A.; Cassano, A. E. *Catal. Today* **1997**, *39*, 219.

(8) Kim, D. H.; Anderson, M. A. *Environ. Sci. Technol.* **1994**, *28*, 479.

(9) Kamat, P. V. *Prog. Inorg. Chem.* **1997**, 44.

(10) Candal, R. J.; Zeltner, W. A.; Anderson, M. A. J. *Adv. Oxidat. Technol.*, in press.

(11) Mandelbaum, P.; Bilmes, S. A.; Regazzoni, A. E.; Blesa, M. A. *Solar Energy* **1998,** *65*, 75.

(12) Shiga, A.; Tshujiko, A.; Ide, T.; Yae, S.; Nakato, Y. *J. Phys. Chem. B* **1998**, *102*, 6049−6055.

(13) Judin, V. P. *Chemistry in Britain* **1993**, *5*, 503.

(14) Brown, G. E.; Henrich, V. E.; Casey, W. H.; Clark, D. L.; Eggleston, C.; Felmy, A.; Goodman, D. W.; Grätzel, M.; Maciel, G.; McCarthy, M. I.; Nealson, K. H.; Sverjensky, D. A.; Toney, M. F.; Zachara, J. M. *Chem. Rev.* **1999**, *99*, 77.

(15) Göpel, W.; Schierbaum, K. D. In *Sensors Vol. 2*, 1991, Göpel, W.; Hesse, J.; Zemel, J. N. Eds.; VCH: Weinheim; p 430.

(16) O'Regan; Grätzel, M. *Nature* **1991**, *353*, 737.
(17) Bach, U.; Lupe, D.; Grätzel, M. *Nature* **1998**, *395*, 183.
(18) Paz, Y.; Luo, Z.; Rabenberg, L.; Heller, A. *J. Mater. Res.* **1995**, *10*, 2842.
(19) Bechinger, C.; Ferrere, S.; Zaban, A.; Sprague, J.; Gregg, B. A. *Nature* **1996**, *383*, 608−610.
(20) Henrich, V. E.; Cox, P. A. *The Surface Science of Metal Oxides* Cambridge University Press: 1996, New York.
(21) Hugenshmidt, M. B.; Gamble, L.; Campbell, C. T. *Surf. Sci*. **1994**, *302*, 329.
(22) Henderson, M. A. *Surf. Sci*. **1994**, *319*, 315.
(23) Brinkley, D.; Dietrich, M.; Engel, T.; Farrall, P.; Gantner, G.; Shafer, A.; Szuchmacher, A. *Surf. Sci.* **1998**, *395*, 292.
(24) Mao, Y.; Schöneich, Ch.; Asmus, K. *J. Phys. Chem.* **1991**, *95*, 10080.
(25) Göpel, W.; Rocker, G.; Feierabend, R. *Phys. Review* **1983**, *28*, 3427.
(26) Yoshimura, N.; Itoi, M.; Sato, S.; Taguchi, H. *Electrical Eng. Japan* **1992**, *112*, 10.
(27) Könenkamp, R.; Wahi, A.; Hoyer; P. *Thin Solid Films* **1994**, *246*, 13.
(28) Xu, W. X.; Zhu, S.; Zhou, J.; Fu, X. C.; Zhao, X. N. *J. Chem. Soc. Faraday Trans*. **1997**, *93*, 4187.
(29) Gerfin, T.; Grätzel, M.; Walder, L. *Prog. Inorg. Chem.* **1996**, *44*, 346.
(30) Casarin, M.; Maccato, C.; Vittadini, A. *J. Phys. Chem. B* **1998**, *102*, 10745.
(31) Bates, S. P.; Kresse, G.; Gillan, M. J. *Surf. Sci.* **1997**, *385*, 386.
(32) Lu, G.; Linsenbigler, A.; Yates J. T. *J. Chem. Phys.* **1995**, *102*, 3005.
(33) Henderson, M. A.; Epling, W. S.; Perkins, C. L.; Peden, H. F.; Diebold, U. *J. Phys. Chem. B* **1999**, *103*, 5328.
(34) Göpel, W.; Anderson, J. A.; Frankel, D.; Phillips, K.; Schäfer, J. A.; Rocker, G. *Surf. Sci*. **1984**, *139*, 333.
(35) Rusu, C. N.; Yates, J. T. *Langmuir* **1997**, *13*, 4311.
(36) Zaban, A.; Meier, A.; Gregg, B. A. *J. Phys. Chem. B.* **1997**, *101*, 7985.
(37) Cao, F.; Oskam, G.; Searson, P. C.; Stipkala, J. M.; Heimer, T. A.; Farzad, F.; Meyer, G. J. *J. Phys. Chem.* **1995**, *99*, 11974.
(38) Boschloo, G.; Fitzmaurice, D. *J. Phys. Chem. B.* **1999**, *103*, 2228.
(39) Mandelbaum, P. A.; Bilmes, S. A.; Regazzoni, A. E.; Blesa, M. A. *J. Phys. Chem. B* **1999**, *103*, 5505.
(40) Mohamed, M. H.; Sadeghi, H. R.; Henrich, V. E. *J. Phys. Chem. B* **1988**, *37*, 8417.
(41) Pétigny, S.; Mostéfa-Sba, H.; Domenechini, B.; Lesniewska, E.; Steinbrunn, A.; Burgeois, S. *Surf. Sci.* **1998**, *410*, 250.
(42) Epling, W. S.; Peden, C. H. F.; Henderson, M. A.; Diebold, U. *Surf. Sci.* **1998**, *412/413*, 333.
(43) Warren, D. **1954**, *X-ray Diffraction Procedures for Polycrystalline and amorphous Materials*, Chapmann Hall, NY.
(44) Hammer, P.; Vitoria, N. M.; Alvarez, F. *J. Vac. Technol. A* **1998**, *16*, 2941.
(45) Jackson, W. B.; Amer, N. M. *Phys. Rev.* **1982**, *25*, 5560.
(46) Alvarez, F.; Sebastiani, M. *J. Appl. Phys.* **1992**, 71.
(47) Sullivan, J. L.; Saied, S. O.; Bertoti, I. *Vacuum* **1991**, *42*, 18.
(48) Atashbar, H. T.; Sun, B.; Gong, W.; Wlodarski, R.; Lamb *Thin solid Films* **1998**, *326*, 238.
(49) Moulder, J. F.; Stickle W. F.; Sobol, P. E.; Bomben, K. D. *Handbook of X-ray Photoelectron Spectroscopy*; Chastain, J., Ed.; Perkin-Elmer Corp. : Prairie, Minnesota, 1992.
(50) Street, R. *Hydrogenated Amorphous Silicon*; Cambridge University Press: Cambridge, 1991.
(51) Pankove, J. I. *Optical Processes in Semiconductor*; Dover Publications, Inc.: New York, 1971.
(52) Mott, N.; Davis, E. A. *Electronic Processes in Noncrystalline Solids*, 2nd ed.; Clarendon Press: Oxford, 1979.
(53) Tang, H.; Berger, H.; Schmid, P. E.; Lévy, F. *Solid State Comm.* **1994**, *92*, 267.
(54) Radecka, M.; Zakrzewska, K.; Czternastek, H.; Stapinski *Appl. Surf. Sci.* **1993**, *65/66*, 227.
(55) Demetry, C.; Shi, X. *Solid State Ionics* **1999**, *118*, 271.
(56) Pan, J. M.; Maschoff, B. L.; Diebolt, U.; Madey, T. E. *J. Vac. Sci. Technol. A* **1992**, *10*, 2470.
(57) Cuerins, H.; Favre, M. *Amorphous Silicon and Related Materials*; Fritzsche, H., Ed.; World Scientific: Singapore, 1988.
(58) Jackson, W. B.; Amer, N. M.; Boccara, A. C.; Fournier, D. *Appl. Opt.* **1981**, *20*, 1333.
(59) Amato, G.; Fizzoti, F. *Phys. Rev. B* **1992**, *45*, 44.
(60) Brinker, C. J.; Scherer, G. W. *Sol−Gel Science*; Academic Press: New York, 1990.
(61) Sanchez, C.; Ribot, F. *New J. Chem*. **1994**, *18*, 1007.
(62) Livage, J.; Sanchez, C. *J. Non-Cryst. Solids* **1992**, *145*, 11.
(63) Bischoff, B. L.; Anderson, M. A. *Chem. Mater*. **1995**, *7*, 1772.
(64) Marchi, M. C.; Bilmes, S. A.; Negri, R. M. *Langmuir* **1997**, *13*, 3665.
(65) Martin, N.; Rousselot, C.; Rondot, D.; Palmino, F.; Mercier, R. *Thin Solid Films* **1997**, *300*, 113.
(66) Anpo, M.; Tomonari, M.; Fox M. A. *J. Phys. Chem*. **1989**, *93*, 7300.
(67) Schvets V. A.; Kazanski V. B. *J. Catal*. **1972**, *25*, 123.
(68) Balachandran, U.; Eror N. G. *J. Mater. Sci.* **1988**, *23*, 2676.
(69) Biersack, J. B.; Haggmark, G. L. *Nucl. Instrum. Methods* **1980**, *174*, 257.